4108

Holz als Roh- und Werkstoff 59 (2001) 104–116 © Springer-Verlag 2001

Damage evolution and acoustic emission of wood at tension perpendicular to fiber

S. Aicher, L. Höfflin, G. Dill-Langer

This paper presents the tracing of damage evolution in spruce loaded in tension perpendicular to fiber direction by means of acoustic emission (AE) analysis. The 2 dimensional burst source location in cross-sectional slabs of boards utilized full wave form recording of AE signals monitored by six simultaneously triggered multiple resonant longitudinal (p–)wave sensors and fast transient recorder PC cards. The location algorithm was based on the minimization of the run time differences between experimental and theoretical signal travel times. The latter accounted for the global polar material anisotropy leading to considerably variable off-axis wave velocities along the wave propagation paths, assumed to be straight; the employed orthotropic on- and off-axis p-wave velocities were obtained experimentally from ultrasound pulse measurements. Below 50% of the ultimate load generally very few burst events were recorded. At further increased load, burst agglomerations were predominantly associated to local areas of elevated stresses here resulting from the specific configuration of anisotropy and loading. For all specimens a distinct burst localisation was obtained in the range of 80 to 90% of the ultimate load, coinciding well with the theoretically highest stressed areas of the fracture plane at brittle failure. The correlation of AE event rates with global strain allowed a tracing of the damage evolution especially when events in confined areas are regarded. Distinct damage localisation was then denoted by a clear AE rate increase, however, not accompanied by a global stiffness change. The investigations revealed that failure of spruce – and most probably of similar softwoods – in tension perpendicular to grain, although being very brittle from a macroscopic perspective, is preceded by progressive and localizing damage evolution on the micro-level which can be traced accurately in space and time by acoustic emission burst source analysis.

S. Aicher (✉), L. Höfflin, G. Dill-Langer
Otto-Graf-Institute,
Department of Wood and Timber Engineering,
University of Stuttgart,
Pfaffenwaldring 4,
70569 Stuttgart, Germany

The financial support of this research work by Deutsche Forschungsgemeinschaft (DFG) through funding of collaborative research centre 381 and hereby of project A8 "Damage and NDT of the natural fiber composite material wood" is gratefully acknowledged.

Schädigungsevolution und Schallemission von Holz bei Zug rechtwinklig zur Faserrichtung

Der Aufsatz berichtet über die Verfolgung der Schädigungsevolution von rechtwinklig zur Faserrichtung zugbeanspruchtem Fichtenholz mittels Schallemissions(SE)-Analyse. Die 2dimensionale Burst-Quellenlokalisierung in Querschnittsscheiben von Brettern erfolgte über die Aufzeichnung der gesamten Wellenform der SE-Signale, die mittels sechs gleichzeitig getriggerter, mehrfach resonanter Longitudinal(p)-Wellen Sensoren und schneller Transientenrecorder-PC-Karten registriert wurden. Der Lokalisierungs-Algorithmus fußte auf der Minimierung der Laufzeitunterschiede zwischen experimentellen und theoretischen Signal-Laufzeiten. Letztere wurden unter Berücksichtigung der globalen polaren Materialanisotropie ermittelt, die zu deutlich veränderlichen Wellengeschwindigkeiten längs der als gerade angenommenen Wellenausbreitungspfade führt; die verwendeten orthotropen on- und off-axis p-Wellengeschwindigkeiten wurden experimentell mittels Ultraschall-Pulsmessungen bestimmt. Unterhalb von 50% der Höchstlast wurden im allgemeinen sehr wenige Burst-Ereignisse aufgezeichnet. Bei weiter erhöhter Last traten Burst-Anhäufungen überwiegend in Bereichen örtlich erhöhter Spannungen auf, die im betrachteten Fall aus der speziellen Konfiguration von Anisotropie und Belastung resultieren. Bei allen Prüfkörpern wurde im Bereich von 80 bis 90% der Höchstlast eine ausgeprägte Burst-Lokalisierung erhalten, die sehr gut mit den theoretisch höchst beanspruchten Bereichen der Bruchfläche beim Sprödbruchversagen übereinstimmte. Die Korrelation der SE-Ereignisrate mit der globalen Dehnung ermöglichte eine Verfolgung der Schädigungsentwicklung, insbesondere wenn Ereignisse in örtlich begrenzten Gebieten betrachtet werden. Eine ausgeprägte Schädigungslokalisierung war sodann durch einen deutlichen SE-Ratenanstieg ausgezeichnet, der jedoch nicht mit einer globalen Steifigkeitsänderung verbunden war. Die Untersuchungen zeigten, daß dem aus makroskopischer Sicht sehr spröden Versagen von Fichtenholz – und sehr wahrscheinlich von ähnlichen Holzarten – bei Zugbeanspruchung rechtwinklig zur Faserrichtung eine progressive und sich lokalisierende Schädigungsevolution auf dem Mikrolevel vorausgeht. Letztere kann in sehr präziser Orts- und Zeitauflösung durch Quellenlokalisierung von Schallemissionen verfolgt werden.

1
Introduction

Cracking and eventually failure due to tension stresses perpendicular to the grain is one of the most important restrictive issues in the processing and use of softwoods. So, for instance, speed and intensity of the drying process are governed by avoidance of excessive crack inducing tensile stress gradients normal to fiber direction. In case of building components, such as curved and pitched cambered glulam beams, tension stress perpendicular to the grain is very often determining ultimate capacity and thus the design load. In-service damage and cracking of solid wood and glulam is predominantely caused by climate induced tension eigenstresses.

The stress distribution in the cross-section of a single softwood board or in several lamellas adhered to glulam is complex in tension perpendicular to the grain due to the polar anisotropy within the cross-section. The latter is finally determined by the sawing pattern of the board, i.e. its location vs. the pith of the original stem (Aicher and Dill-Langer 1996). Further, the stochastic defect distribution of the material interacts with the stress distribution (Dill-Langer and Aicher 1997). As the failure occurrence in case of tension perpendicular to grain is very brittle, in-situ monitoring of the fracture process by SEM or CLSM microscopy is confined to very small specimens with edge lengths of a few millimetres (Dill-Langer et al. in press). For specimens at the macro-scale and finally for construction elements acoustic emission (AE) monitoring represents probably the most promising NDT tool to gain insight into the damage evolution of the regarded complex load-material configuration (Aicher and Dill-Langer 1999).

Burst source monitoring and location is state-of-the-art for production control or in-situ building component survey for quasi isotropic materials like steel (e.g. Sison et al. 1998). In wood science the first application of the acoustic emission technique to detect fracture development was performed by Adams 1969. Since then the prevailing and most advanced applications of AE monitoring were performed in the field of wood drying (i. a. Becker 1982; Honeycutt et al. 1985; Booker 1994; Lee 1994; Schniewind et al. 1996). The general aim of these investigations is to establish correlations between AE emissions and surface checks, finally to be used for active drying control.

The investigations described in this paper are addressed to two major issues: location of burst signals within the radial-tangential growth plane of (soft)wood loaded in tension perpendicular to the grain and correlation of the located burst signals to global stress-strain behavior.

2
Material and specimen built-up

The reported investigations comprised four test volumes I–IV of European spruce (*Picea abies*), cut from different boards. In the following, the test volumes are referred to as specimens, too, whereas the "complete specimens" consisting also of specific necked on-gluings (see below) are termed "necked tension specimens". All four specimens with almost identical dimensions were macroscopically defect free (Figs. 1 and 2), and so can be termed clear wood. The specimen width w, actually representing the thickness of the boards from which the slab-like specimens were cut, was 45 mm and specimen length l, the wide side of the boards, was 180 mm. Thickness t of the test volume, the dimension parallel to fiber, was 31 mm. It should be stated that dimension t, from an analysis point of view, is of minor importance in this investigation as wave propagation and stress distribution in an approximation was assumed as a plane problem in the radial (r)-tangential (t) plane.

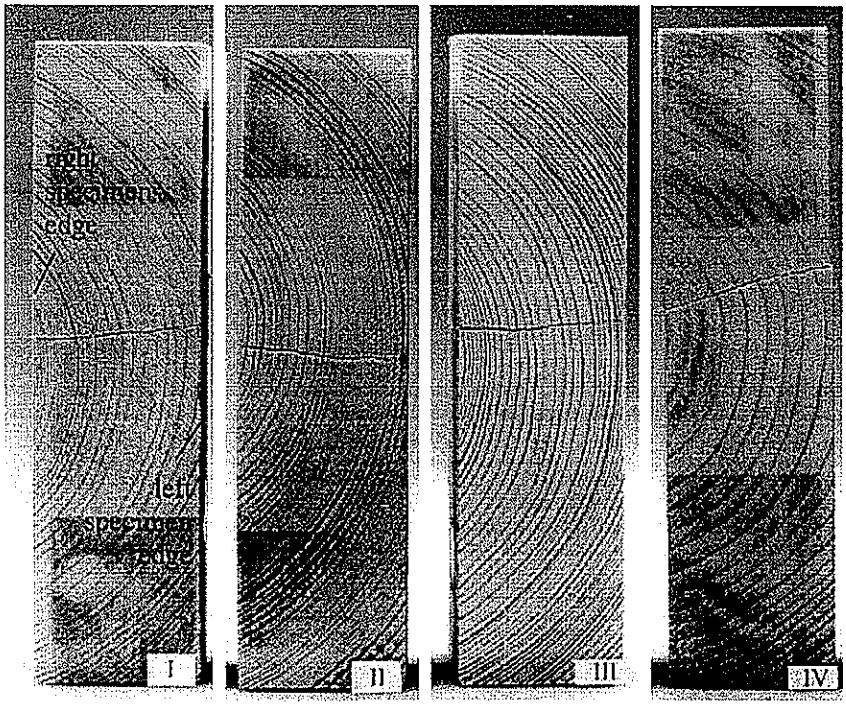

Fig. 1. Front view of the four investigated test volumes cut from different spruce boards, illustrating the respective annual ring configuration (pith location, ring width) and the position of the failure planes obtained in the tension loading
Bild 1. Vorderansicht der vier geprüften, aus verschiedenen Fichtenholzbrettern geschnittenen Testvolumina; man beachte die jeweilige Jahrring-Orientierung (Markröhrenlage, Jahrringbreite) sowie die Lage der in den Zugversuchen erhaltenen Bruchebenen

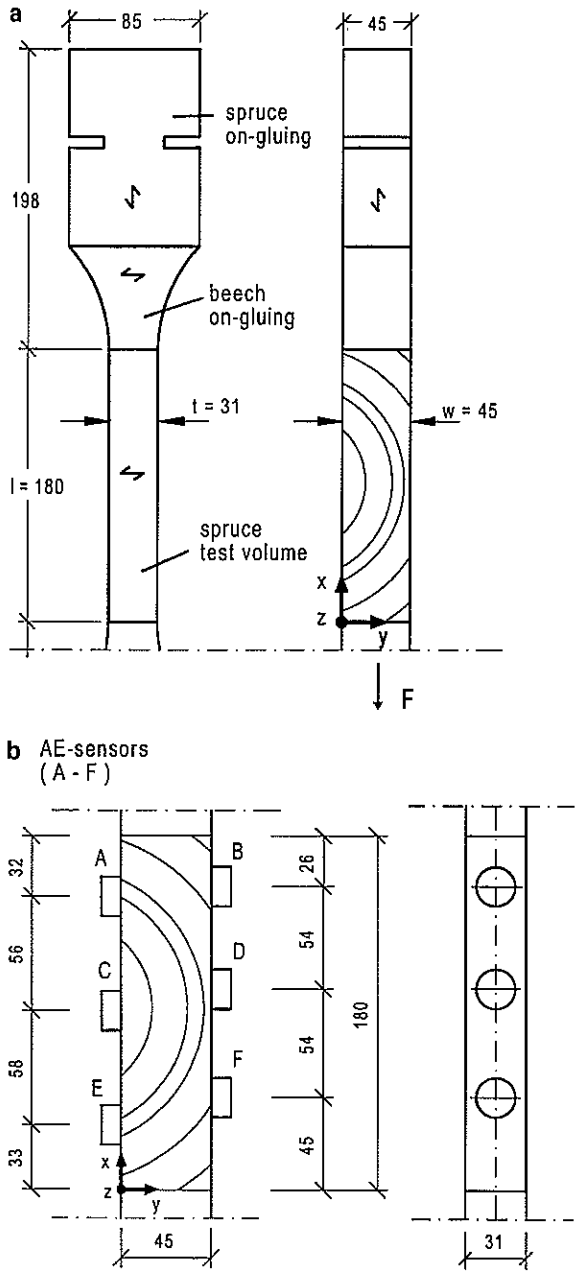

Fig. 2a, b. Built-up of necked tension specimen *a* and location of AE sensors *b* at the test volume
Bild 2a, b. Aufbau des schulterstabförmigen Zugprüfkörpers *a* und Anordnung der SE Sensoren *b* am Prüfvolumen

The four specimens I–IV differed considerably with respect to wood density, location of pith, ring width (measured at mid-length across specimen width) and portion of compression wood. Table 1 contains a compilation of the respective individual specimen data.

One of the four specimens, No. II, contained a rather considerable amount of compression wood especially in the vicinity of the "lower left" corner (see Fig. 1). For all slabs the annual ring orientation was rather symmetric versus mid-length of the slab; hereby eccentricity of the pith, denoted by dimension e (see Fig. 7) was only a few (0.5–9.5) millimetres. However, there was quite some difference between the slabs regarding distance d (22 to 48 mm) of the stem axis (pith) to the so-called "right", closer to pith oriented board side.

In order to avoid damage resp. failure in the interface between test volume and on-gluings, necessary to transfer the load, a specific necked specimen built-up as shown in Fig. 2a was developed. In order to obtain a rather smooth stress transition from the prismatic test volume to the on-gluings, special hybrid necked on-gluings made of two wood species were used. The necked part adjoining to the test volume, comprising the crucial interface, was made of beech wood whereby fiber orientation coincided with that of the test volume. As stiffnesses of beech and spruce are in the same order of magnitude, no pronounced stress concentration occurs in the vicinity of the interface; further tension strength perpendicular to grain of beech is roughly 1.5 to 2 times higher compared to spruce.

3
Test configuration

The necked specimens were conditioned in constant climate of 20°C/65% RH for several weeks to weight equilibrium and kept in climatised conditions until immediate test begin; then the AE sensors were adhered to the specimens. The tests were conducted at about 20°C in a non-climatised test room.

The number of necessary sensors, resp. their spacing was evaluated for the specific configuration of AE equipment and settings (i. a. trigger threshold, amplification) in preliminary tests. There it was found that due to the high signal attenuation of p-waves in the radial-tangential growth plane of spruce (and wood in general), the distance between burst source and sensors should not exceed about 100 mm. The locations of the three respective AE sensors along the center-lines of both side grain faces are shown in Fig. 2b; the specified dimensions are averages of the four

Table 1. Material properties of specimens I–IV
Tabelle 1. Materialeigenschaften der Prüfkörper I–IV

Specimen No. –	Density ρ_{12} [kg/m^3]	annual ring width b_r				location of pith[1]		apparent MOE[2] perp. to grain $E_{90,app}$ [N/mm^2]	tension strength perp. to grain $f_{t,90}$ [N/mm^2]
		mean [mm]	C.O.V. [%]	min [mm]	max [mm]	e [mm]	d [mm]		
I	463	1.77	56.7	0.3	3.8	1.5	33	191	1.60
II	505	1.39	40.0	0.5	2.6	−9.5	35	219	2.26
III	480	1.80	39.5	0.9	3.4	0.5	48	209	2.35
IV	407	3.79	37.2	2.0	6.5	−3.5	22	180	2.40

[1] see Fig. 7; [2] determined from load range 0.05–0.25 $f_{t,90}$

specimens, the individual values varied only by very few millimetres. The oppositely arranged sensors A and B, C and D resp. E and F were not mounted exactly opposite but throughout with some (3–13) millimetres distance along specimen length.

The determination of the global or apparent stiffness $E_{90,app}$ parallel to load axis of the test volume was measured by two LVDTs adhered diagonally opposite onto the side faces of the beech on-gluings; the center of the fixation had a nominal off-set of 10 mm to the interface between on-gluings and test volume. Both ends of the necked tension specimens were mounted via cardanic hinges to the grips of a stiff screw driven test machine. The tests were performed in displacement control at a constant cross-head speed of 0.4 mm/min. The times to failure of specimens I–IV were 536, 560, 584 and 621 seconds, so in average 575 seconds. The obtained tension strengths $f_{t,90}$ varied from 1.6 to 2.4 N/mm^2. Apparent MOEs $E_{90,app}$ determined from the almost linear loading regime between 5 to 20% of tension strength varied within a narrow range of about 180 to 220 N/mm^2 (above 0.20 $f_{t,90}$ an increasing non-linearity due to visco-elasticity is encountered); detailed results are compiled in Table 1.

4
Stress analysis

In order to obtain some idea of the most probable source region of AE signals, assumed to be associated with areas of locally increased stresses, linear elastic 2D finite element simulations of the specimens were performed. The 2D plane stress analysis was based on a polar anisotropic constitutive law assuming in an approximation a smeared homogeneous continuum. The origin of the polar material co-ordinate system is defined by the pith location parameters e and d (see Fig. 7) specified for the respective specimens in Table 1. The computations were performed with the on-axis material parameters (stiffnesses in N/mm^2)

$$E_r = 1200, \quad E_t = 800, \quad G_{rt} = 50, \quad \nu_{rt} = \nu_{tr} E_t / E_r = 0.35;$$

the stated values affect the analysis solely by the prescribed ratios $G_{rt}:E_t:E_r = 1:16:24$ which conform roughly to the means of literature given ranges.

The polar material anisotropy in combination with the applied uniaxial off-axis loading results, as mentioned in the introduction, in an extremely uneven stress distribution within the specimen. The specific reason for the stress variations along width and length of the specimen (see below) stems from the very low ratio of shear to normal stiffnesses inducing a pronounced shear coupling effect in the global off-axis loading. Details and empirical verifications by means of direct strain measurements are given in Aicher et al. (2001). Following, solely results for σ_x, i.e. the stress component parallel to load direction, regarded most decisive for tension failure perpendicular to the grain, are presented.

Figure 3a shows, exemplarily for the case of specimen I, distributions of stress component σ_x along specimen length at different sections resp. edges y = const. of width. The analysis yields two pronounced stress peaks at the "left" and "right" edge, roughly at mid-length. Between the two peaks, a sloping stress valley is obtained. The stress peak at

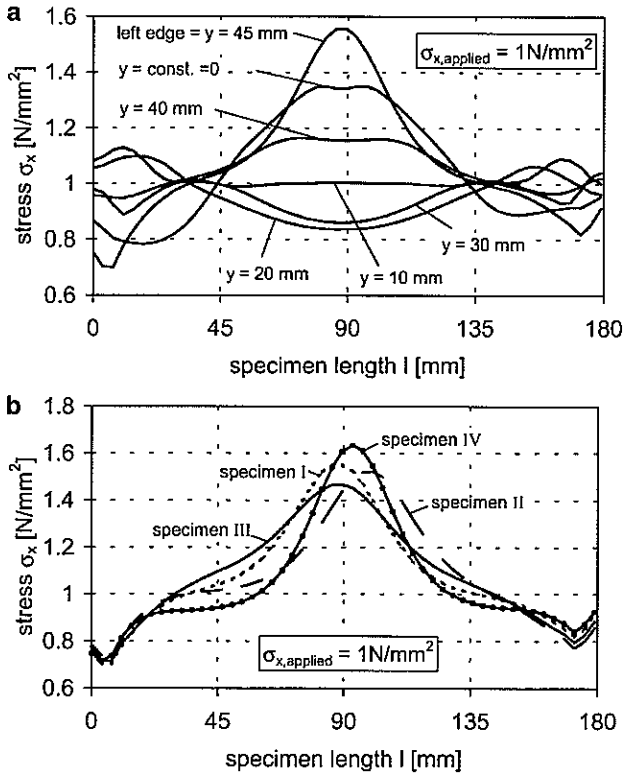

Fig. 3a, b. Distribution of stress σ_x perpendicular to grain along specimen length; *a* in sections y = const. = 0, 10, 20, 30, 40 and 45 mm (here: specimen I) *b* at edge y = const. = 45 mm of specimens I to IV

Bild 3a, b. Spannungsverläufe σ_x rechtwinklig zur Faserrichtung über die Prüfkörperlänge; *a* längs der Schnitte y = const. = 0, 10, 20, 30, 40 und 45 mm (hier: Prüfkörper I) *b* längs der Kante y = const. = 45 mm der Prüfkörper I bis IV

the "left" edge is slightly higher compared to the opposite one at the "right" edge, whereby maximum values are about 1.6 and 1.4 times higher compared to applied (here: unit) tension stress. The lower plateau-like stress peak at the "right" edge stretches roughly 30 mm in loading direction, whereas the sharper peak at the "left" edge can be smeared roughly over 10 to 15 mm. Figure 3b illustrates the difference of σ_x stress distributions between specimens I to IV by means of the stress curves along the "left" edge. It can be seen that the peak stress levels of specimens I and II are rather similar due to comparable pith distances d, whereas the peak locations differ by about 20 mm due to diverting eccentricities e (see Table 1). Specimen IV with the smallest off-set d of pith from the "right" edge, i.e. with highest curvature of the polar material co-ordinate system, gives the highest stress peak, whereas specimen III, showing, the largest d value, reveals the lowest peak.

5
Acoustic emission monitoring

5.1
Equipment, triggering and signal storage

The recording of the AE signals was performed by means of a special AE recording system consisting of three equal

and coupled fast transient recorder PC-cards capable to digitise and store AE waveforms. The features of the cards were two channels each with a digitisation rate of 20 MHz and 12 bit amplitude resolution. For detection of the acoustic emissions six equal multiple resonant piezoelectric transducers (sensors) for longitudinal waves with a maximal gain between 40 and 450 MHz were employed; the resonance maximum of the sensors A–F was 150 MHz. The suitability of multi-resonant transducers of the chosen frequency domain, as for instance compared to broadband transducers, was evaluated for the specific test configuration in several preliminary investigations. The flat circular coupling surface of the cylindrically shaped sensors had an outer diameter of 20 mm with an interior effective sensor diameter of 16 mm. The coupling of the sensors to the side-grain faces of the wood specimens was performed by means of a cold setting removable PVac adhesive; no specific pressure was used during application and curing time. The captured signals were amplified by a factor of 5000 and filtered by a band pass between 10 kHz and 1 MHz.

The triggering of all sensors resp. signal storage commenced simultaneously for all channels when the trigger condition was fulfilled for the first time at one of the six sensors. Based on preliminary investigations the employed trigger condition was of slope type with a 2 volt rise within 20 microseconds. The pre-trigger time, i.e. the time span for which recording of each channel is continuously buffered in the memory in order to capture the whole signal, which may start in case of the first recording channel(s) well before the rather deliberately chosen trigger threshold, which was set to 10% of the whole recordable signal time; the latter comprised maximally 1.68 microseconds. The minimal time gap between two recorded AE burst events – eventually received at all six sensors – was 0.21 seconds. It should be mentioned that due to the chosen test set-up consisting of resonant transducers, the specific amplification factor, the slope type trigger condition and the time lag between recording of successive events, an unknown number of events of other frequency domains, of low amplitude resp. of rapid succession is not registered.

5.2
Picking of AE signals

The picking of the signals, i.e. the determination of the signal on-set or start times relative to zero trigger time in the post-test evaluation was performed in two stages. In the first stage an automatic picker program[1] was employed recommending signal on-set times. All recommended times were then checked and in most cases adjusted with respect to consistent below stated definitions for signals and on-set times.

In this investigation each signal used for the location evaluation had to conform to two conditions, being

- amplitude-noise ratio $r = A_{max}/N_l \geq 5$ and signal length ≥ 0.5 µs whereby the following definitions hold (compare Fig. 6):
- maximum amplitude A_{max} is the highest absolute value (signal voltage) measured from zero to peak amplitude, noise level N_l of the continuous background noise is defined as half of the absolute symmetric bandwidth parallel to zero amplitude, and signal or event length is defined as the time span between first and last signal amplitude exceeding noise level.

The on-set or start time of a thus defined event relative to zero trigger time was then determined by the point of intersection between the zero line and the tangent line to the slope of the first wave peak of the signal. A continuous off-set of noise from zero line has to be eliminated before evaluation. Examples of above definitions are given below.

6
Signal characteristics

Figures 4a–f reveal the wave form features, i.e. the complete signals, registered at the six sensors A–F for a typical burst signal (here termed event 1) which forwards at all six sensors well evaluable signals. Event 1, according to the plane location algorithm, was located roughly at the center of the specimen. For a clear comparison, all individual signals A–F are given with equal amplitude and time scales. The fastest and strongest signals were received at sensors D and C, whereby sensor D was triggering first ($j = 1$). The time lag of sensor C vs. sensor D is very small (3.4 µs). This means that the emission is located somewhere between both sensors if we assume roughly comparable effective velocities. Both signals C, D are rather symmetric vs. noise level and have maximum amplitudes A_{max} of about 3.5 and 1.5 V. The rise time R_t of both signals is about 13 µs (D: 11.2 µs; C: 14.2 µs) and thus very short; R_t describes the time span between clearly identified signal onset, as defined here, and maximum amplitude A_{max}. The signals received at sensors A and B resp. at E and F show smaller amplitudes and, differently accentuated, are more diffuse. However, unambiguous determination of signal on-set, according to the conditions specified, is possible in all cases, even for signal F, distinguished by the smallest amplitude-noise ratio $r = 5.5$.

Figures 5a–f and 6a–f show at different scales the waveforms of another burst event (here termed event 2) located rather close to one of the narrow edges in vicinity of transducer A. Figures 5a–f, distinguished by equal amplitude and time scales for the signals at all six sensors immediately reveal the problems encountered in case of such a type of event. The signals received at the different sensors differ very distinctly with respect to amplitude-noise ratio making it impossible to evaluate the signals at equal scales. Figures 6a–f give the signals of event 2 at individual amplitude and time scales, now enabling the application of the specified signal validity resp. on-set time definitions. Figures 6a–d in a qualitative manner reveal for signals A to D the appropriateness of the chosen signal on-set time definitions. In the same sense, Figures 6e, f show for the case of signals E and F how the chosen definitions exclude signals with clear on-set interpretation problems, finally leading to wrong location results.

[1] obtained by courtesy of our colleagues Dr. Große, Dr. Weiler from sub-project A6 in the SFB 381

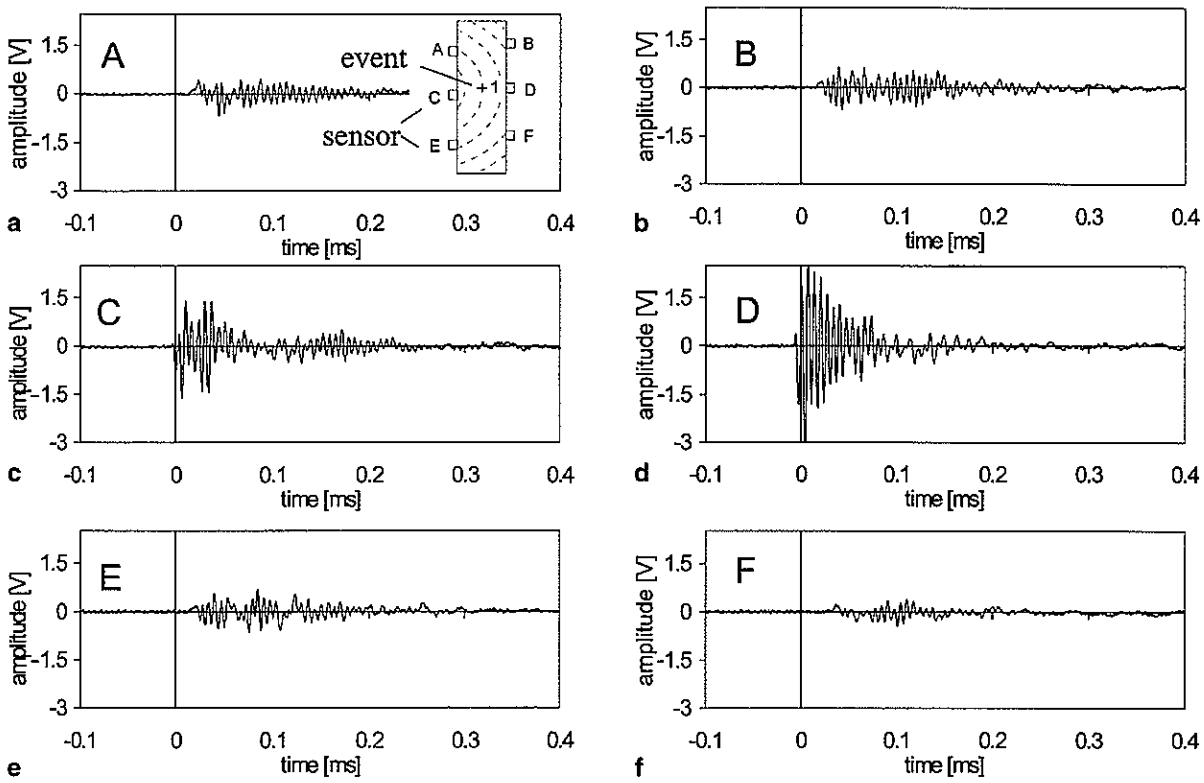

Fig. 4a–f. Typical AE wave forms received at sensors A–F in case of a burst event located rather centrically in the specimen

Bild 4a–f. Typische, an den Sensoren A-F erhaltene SE Wellenformen im Falle eines weitgehend zentrisch im Prüfkörper liegenden Burst Ereignisses

7
Burst source location

7.1
Location algorithm

The algorithm used for the burst source location is based on a least square minimisation of the differences between recorded and theoretical signal travel times resp. more precise on normalised travel time differences

$$\mathrm{Res}(x,y) = \min \sum_{j}^{n} \Delta T_{ij}^2 \quad 1 \le j \le n = 6 \qquad (1)$$
$$0 \le x = x_i \le l,\ 0 \le y = y_i \le w$$

where

$$\Delta T_{ij} = \left(\Delta t_{ij,\mathrm{theor}} - \Delta t_{ij,\mathrm{exp}}\right)/\Delta t_{ij,\mathrm{exp}},$$
$$\Delta t_{ij,\mathrm{theor}} = T_{ij,\mathrm{theor}} - T_{i,j=1,\mathrm{theor}},$$
$$\Delta t_{ij,\mathrm{exp}} = \Delta T_{ij,\mathrm{exp}} - \Delta T_{i,j=1,\mathrm{exp}}.$$

Time $T_{ij,theor}$ represents the theoretical travel time from location $x = x_i$, $y = y_i$ to sensor j along path length l_{ij} where $j = 1, 2 \ldots 6$ denotes the first, second resp. sixth triggering sensor and i is the respective signal number (see Fig. 7). The semi-empiric calculation of the theoretical travel times is outlined below. Time $\Delta T_{ij,exp}$ is the experimental time off-set of signal resp. sensor j vs. trigger time zero set by sensor $j = 1$.

The actual minimisation of the residuum was performed as a grid search within the cross-sectional area of the specimen.

7.2
Effective p-wave velocities in the radial-tangential plane

For calculation of the theoretical travel times $T_{ij,theor}$, plane longitudinal waves and straight wave paths between AE source i and sensors j were assumed. It should be stated that the latter assumption due to the polar anisotropic material may not necessarily give the shortest travel time when considering curved paths, too. The determination of the theoretical travel time of an ultrasound signal from an assumed burst location x_i, y_i to a deliberate sensor j along a straight line l_{ij} necessitates off-axis ultrasound velocities $v(\varphi)$ at deliberate off-axis angles φ relative to the orthogonal on-axis material co-ordinate system defined by the radial resp. tangential directions r and t. As off-axis angle φ in general is changing continuously along path l_{ij} depending on path orientation and pith location, what is illustrated schematically in Fig. 7, the effective ultrasound velocity v_{eff} can be written as

$$v_{\mathrm{eff}} = \frac{1}{\ell_{ij}} \int_{\ell_{ij}} v(\varphi)\,\mathrm{d}s \qquad \mathrm{d}s = \mathrm{d}\varphi \cdot \frac{1}{\dfrac{\mathrm{d}\varphi(s)}{\mathrm{d}s}}. \qquad (2)$$

Another effect which could influence effective velocity, too, is dispersion, where wave velocity becomes a function of frequency. In this paper it is assumed that phase velocity is

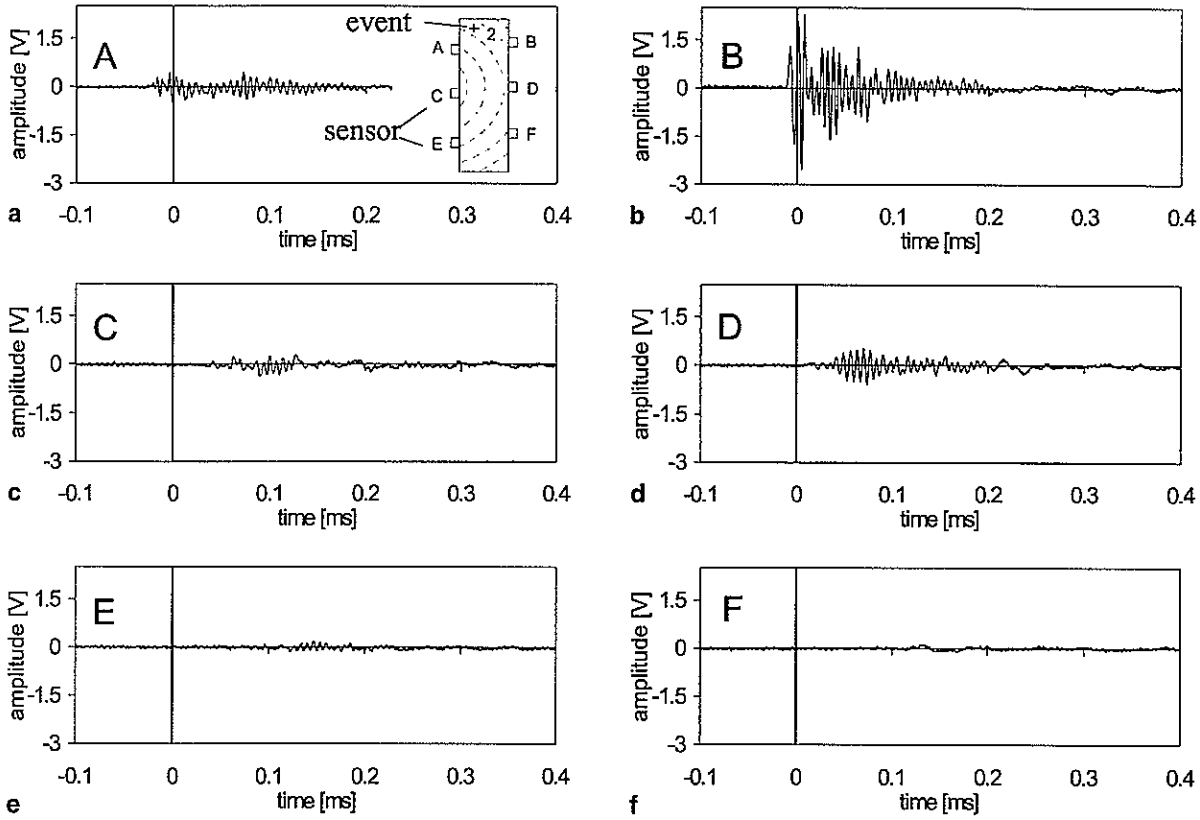

Fig. 5a–f. Typical AE wave forms received at sensors in case of a burst event located close to one of the narrow edges of the specimen cross-section

Bild 5a–f. Typische, an den Sensoren A–F erhaltene SE Wellenformen im Falle eines Burst-Ereignisses nahe einer Schmalkanten des Prüfkörperquerschnitts

independent of frequency, thus identical to group velocity of the wave group of a signal, i.e. no dispersion exists.

In order to minimise location errors induced by incorrect wave velocities, the recommendation by Baron and Ying (1987) to employ measured velocities rather than published values or velocities derived from stiffnesses was followed up. The ultrasound velocities in the orthogonal radial and tangential on-axis directions resp. in off-axis orientations, enclosing an angle φ with the radial direction, were determined experimentally by ultrasound (US) pulse measurements. The latter investigations were performed with small defect-free specimens of European spruce wood (picea abies) of different densities ρ_{12} from 450 to 530 kg/m^3 and mean annual ring widths b_r ranging from 1.4 to 2.3 mm. The sizes of the prismatic specimens with side lengths in r– and t–direction of 22 to 30 mm (thickness: 10 mm) were chosen in order to ensure quasi-orthogonality of the radial and tangential directions hereby minimising the influence of the curvature of the annual rings, i.e. of the actual polar anisotropy. The central frequency of the generated pulses was 350 MHz; a detailed description of the investigations and comparisons with results from ultrasound spectroscopy resp. with theoretical velocities based on solutions for wave propagation in anisotropic media is given in a separate paper.

Figure 8 depicts the results from the ultrasound pulse method related to a wood moisture content of 12%. It can be seen that density has no significant influence on p–wave velocity (and neither has annual ring width). However, there is a considerable influence of the off-axis angle φ between the direction of wave propagation and the radial on-axis material direction r. In order to interpolate between the measured data points, the dependency of off-axis p-wave velocity on off-axis angle φ was approximated by a polynomial function of sixth order in φ. The fitted function gives for the ultrasound velocity maxima in radial and tangential on-axis directions:

$$v(0) = 1865\,\text{m/sec} \text{ resp. } v(90) = 1593\,\text{m/sec}.$$

In the range of about $\varphi = 48$ degrees minimal p–wave velocities of about 1460 m/sec are obtained. The mean velocity throughout the whole on-off-axis regime is

$$\bar{v}(\varphi) = 1/90 \int_0^{90} v(\varphi)\mathrm{d}\varphi = 1603\,\text{m/sec}.$$

Due to the considerable variation in off-axis velocities, effective p–wave velocity v_{eff} depends pronouncedly on the specific path orientation and length in the polar anisotropic continuum. Generally speaking, the variability of angle φ grows with increasing path length due to the globally curved material co-ordinate system of the boards cross-section. For the regarded test configurations, effective velocities from a deliberate burst location to the six sensors can well differ by about 25% being close to the extreme values of the on- and off-axis velocities. This

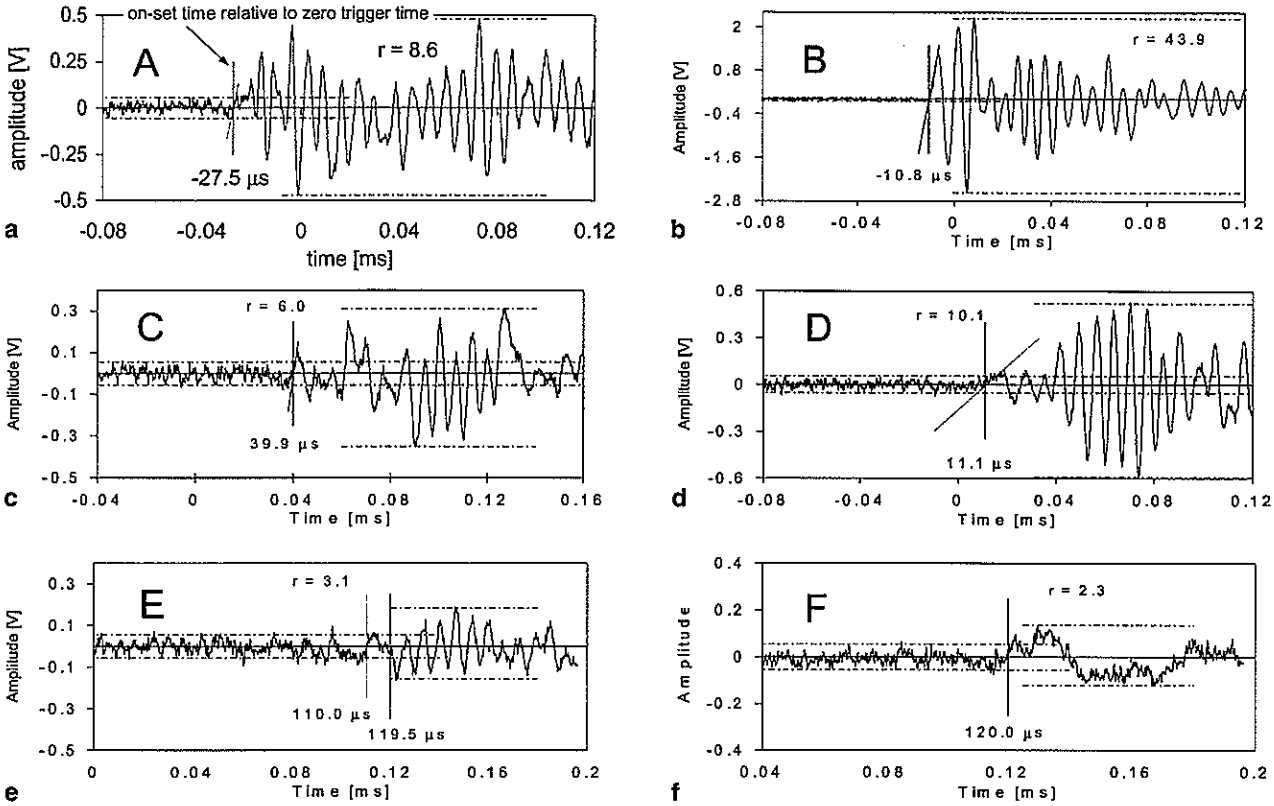

Fig. 6a–f. Application example of here defined criteria for AE signal validity and on-set time

Bild 6a–f. Anwendungsbeispiel der hier definierten Kriterien für die Gültigkeit und die Erst-Einsatzzeit eines SE Signals

underlines the high relevancy of precise sound velocities for burst source location.

8 Location results

Table 2 contains a compilation of the numbers of AE events located within specific specimen areas and load ranges. Figures 9a–d show the location results within the cross-sectional plane of specimens I to IV as a sequence of four respective charts; the located burst events are given for the successive load ranges of 0 to 50%, 50 to 80%, 80 to 90% and 90 to 100% of ultimate load F_u. According to the 2D nature of the performed location, the burst events in each chart represent the approximate projections of the AE signals into the middle plane of the

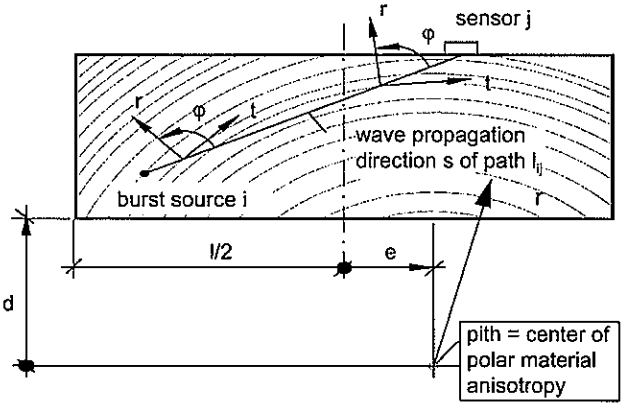

Fig. 7. Variation of off-axis angle φ along a deliberate straight wave propagation path; definition of pith locus co-ordinates e and d

Bild 7. Veränderlichkeit des off-axis Winkels φ längs eines beliebigen geraden Wellenausbreitungspfades; Definition der Markröhren-Lagekoordinaten e und d

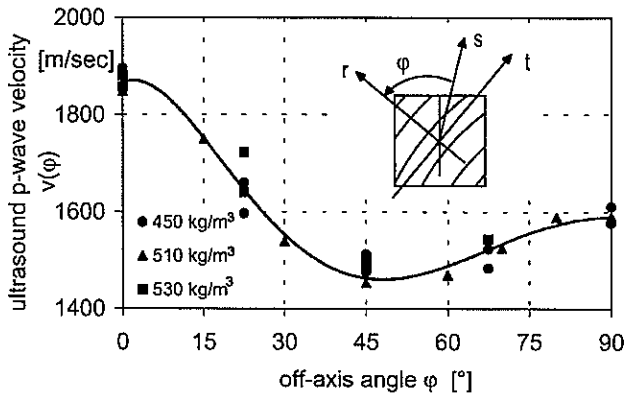

Fig. 8. Measured ultrasound p-wave velocities of spruce in the radial-tangential growth plane depending on off-axis angle φ

Bild 8. Gemessene Ultraschall p-Wellengeschwindigkeiten für Fichte in der Radial-Tangentialwuchsebene in Abhängigkeit vom off-axis Winkel φ

Table 2. Number of AE events of specimens I–IV within specific areas and load ranges
Tabelle 2. Anzahl der SE Ereignisse der Prüfkörper I–IV innerhalb ausgezeichneter Flächen und Lastbereiche

	Number of AE events per specimen							
	I		II		III		IV	
	–	%	–	%	–	%	–	%
total specimen[1)]	144	100	152	100	68	100	77	100
events located in the interfaces	7		98		21		2	
events located within a band of ±8 mm of the failure plane	119	82.6	49	32.2	31	45.6	62	80.5
load range[1)]								
0–0.5 F_u	1	0.7	17	11.2	6	8.8	0	0
0.5–0.8 F_u	27	18.7	57	37.5	23	33.8	10	20.8
0.8–0.9 F_u	61	42.4	34	22.4	21	30.9	18	23.4
0.9–F_u	55	38.2	44	28.9	18	26.5	43	55.8

[1)] interface events excluded

specimens. Further, it should be mentioned that all events located exactly in the interfaces between test volume and on-gluings are not given in the charts as these events are not related to the investigated damage evolution within the test volumes. The number of events located in the interfaces varied considerably for the different specimens I to IV (Table 2).

Up to about 50% of ultimate load almost no burst event occurred at three of the four specimens (I, III and IV). In detail, the first respective event of specimens I, III and IV occurred at a stress level of 40, 27 and 55% and the number of events up to 0.5 F_u was 1, 6 and 0 for specimens I, III and IV. As exception hereof, specimen II showed a considerable number (17) of AE events up to 0.5 F_u being distributed rather diffusely within the cross-section. It is assumed that the reason for these early emissions consists in the mentioned pronounced percentage of compression wood of specimen II, being the only obvious difference compared to the other specimens.

In the load range of 0.5 to 0.8 F_u, emission activity occurred for all four specimens whereby the number of events differed pronouncedly, ranging from 10 in case of specimen IV to 57 for specimen II. Further, the four specimens differed considerably with respect to the locations of the events. In case of specimen I, almost all events occurred at the "left" face[2] of the specimen within the highest stressed area as outlined above. The compression wood specimen II forwarded a completely different spatial burst evolution whereby burst locations at first glance appear to be distributed rather diffusely within the specimen. However, most of the signals can be grouped into four clusters CL1 to CL4 as indicated in Fig. 9b. The three burst clusters CL1, CL2 and CL3 are located in the two opposite peak stress areas at the "left" and "right" specimen faces and cluster CL4 can be associated with areas of high compression wood percentage. The term "cluster" is used here in a qualitative sense for areas of increased spatial density of AE sources; a more exact and quantitative analysis of cluster formation and evolution is beyond the scope of this paper and shall be subject of a separate study. Specimen III shows a band of burst emissions with a width of about ±10 mm around the later failure plane. In case of specimen IV one concentrated burst cluster is located in the peak stress areas at the "left" specimen face close to the intersection of the failure plane with the side face.

In the load range of 0.8–0.9 F_u specimens I and II showed a distinct localisation of the acoustic emissions in a very small area (about 5–10 mm^2) at the intersection of the latter failure plane with the "left" specimen face. This intersection and the opposite one at the "right" specimen face following are termed "left" and "right" crack plane on-sets. In case of specimen IV, in addition to the already encountered cluster at the "right" face a second area of increased event density evolved at the "left" crack plane on-set. For specimen III, the feature of the located burst events differs slightly from the other specimens; here events are located loosely around both crack plane on-sets but also diffusely within the specimen.

In the finally regarded load range of 0.9 F_u to ultimate load, where brittle failure occurred, all four specimens showed a very high concentration of the localised AE events in closest vicinity of the failure plane. In case of specimens I and II the localisation occurred exclusively at the higher stressed "left" crack plane on-set. For specimen III the situation is similar, however, the event localisation is not solely at the crack plane on-set; several burst signals follow the fracture plane up to about mid-width of the specimen. For specimen IV the emissions are located at both crack plane on-sets as in the preceding load range.

The presented location results reveal that on-sets of failure planes can be estimated in a rough guess, depending on the material variability, within the load range of 0.5–0.8 F_u. A distinct localisation of the nucleation areas of the failure plane is confined to the load range of 0.8 to 0.9 F_u. The accuracy of the location of the intersections of the failure plane with the side faces underlines the validity of the employed location algorithm based on off-axis p-wave velocities in combination with straight wave propagation paths.

[2]According to the 3D structure of the specimens, the so-called "right" and "left" edges of the cross-section are referred to as "right" and "left" faces.

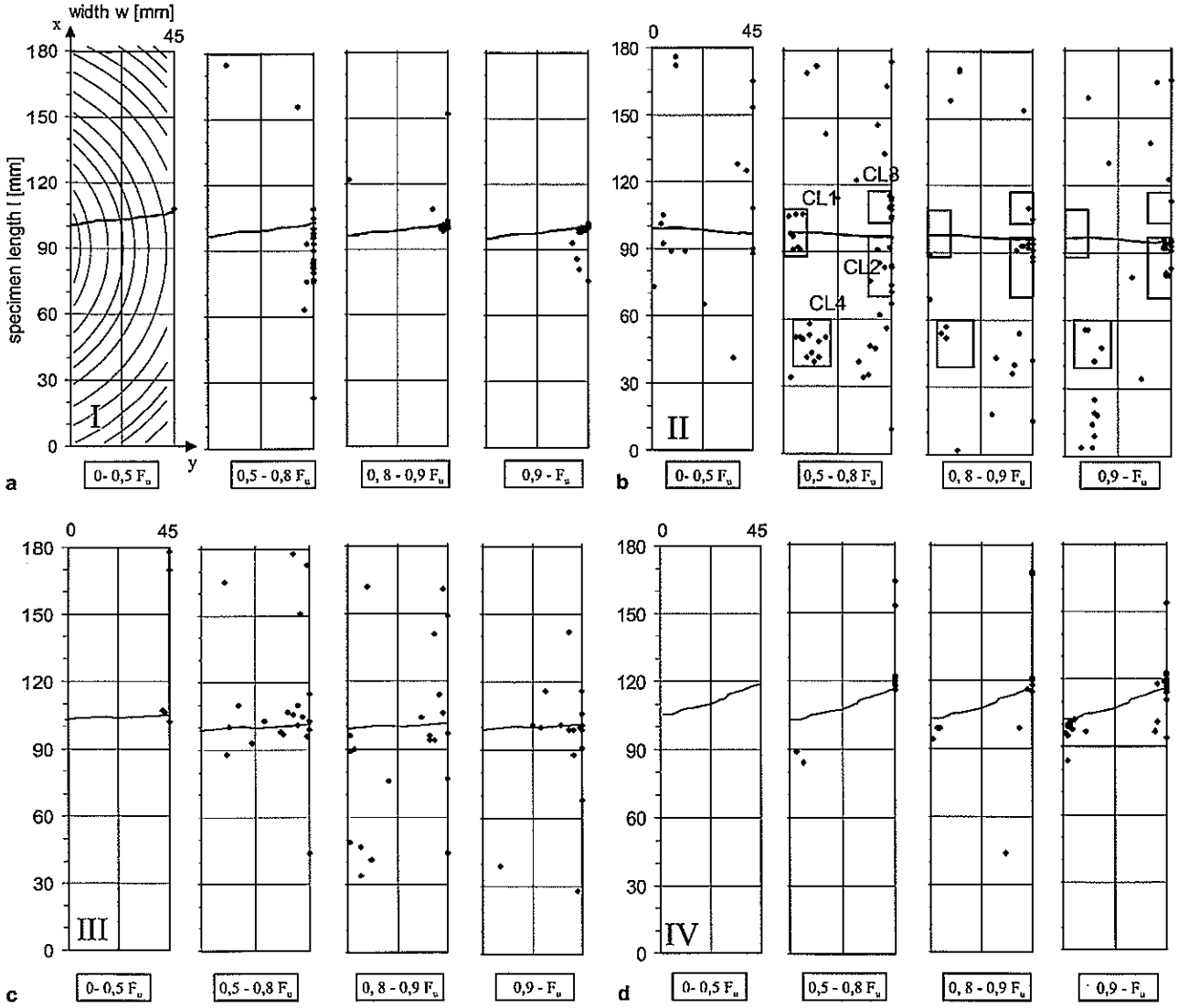

Fig. 9a–d. Located burst sources of specimens I to IV *a–d* at successive load ranges of 0 to 50%, 50 to 80%, 80 to 90% and 90 to 100% of respective ultimate load

Bild 9a–d. Lokalisierte Burst-Quellen der Prüfkörper I bis IV *a–d* in aufeinanderfolgenden Lastbereichen von 0–50%, 50–80%, 80–90% und 90–100% der jeweiligen Höchstlast

9
Damage indication by AE event rate

The question arises whether the discrete AE event rate, i.e. the number of AE events per global strain or stress increment, resp. the slope of the curve of accumulated AE events vs. strain or stress, gives a clear indication of the progress of damage. Figures 10a–d present for each specimen I to IV all registered AE events per strain increment $\Delta\varepsilon = 0.08‰$; the interface bursts are excluded as in the previous chapter. As all events within the continuum are taken into account (alternatively, solely AEs within specific areas might be considered, see below), the rate is termed global discrete AE event rate. Further the global cumulative AE event curves and the global stress-strain relations are given. Two different discrete rate or cumulative curve features can be distinguished.

In case of specimens I and IV, Figs. 10a and d, the discrete AE rates, resp. the slopes of the cumulative curves, show, differently accentuated, a pronounced increase at a certain strain or stress level. However, the global stiffness curve reveals no or almost no (IV resp. I) discontinuity within the general non-linearity. The point of AE event rate change, which at first sight may not be fully obvious from the global discrete rates in case of specimen IV, however, can be defined rather clearly from a bilinear approximation of the cumulative AE curve, as indicated by the thin lines. The slope changes in case of specimens I and IV occur at 80 and 90% of ultimate strain resp. at 90 and 95% of global strength. For specimen II no noticeable change of cumulative slope can be observed at all. Specimen III, Fig. 10c, reveals a significant change of global AE event rate, resp. of cumulative event slope, only at a very late loading stage of about 95% and 97% of ultimate strain resp. stress.

So it can be stated, based on the four investigated specimens, that pure event counting as well as correlations

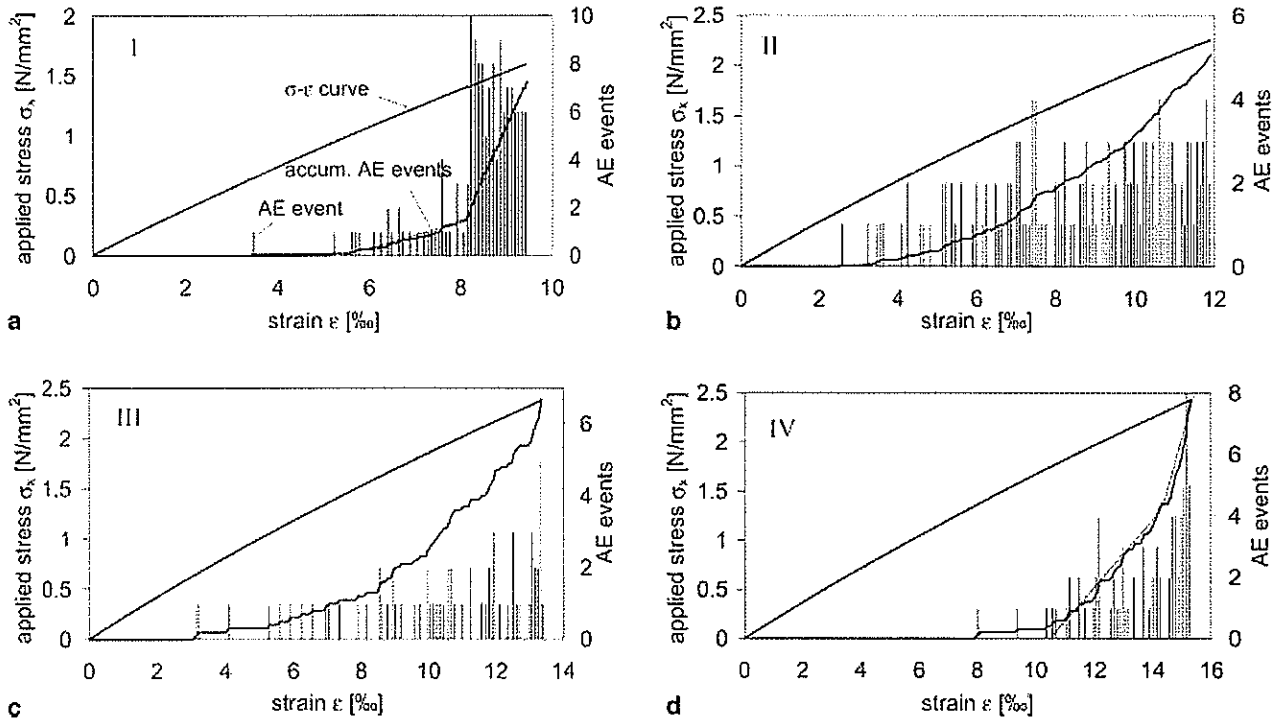

Fig. 10a–d. Entity of registered AE events per strain increment $\Delta\varepsilon = 0.08‰$ (termed: global discrete AE event rate) of specimens I to IV *a–d*; also given are global cumulative AE event curve and global stress-strain curve

Bild 10a–d. Gesamtheit der registrierten SE Ereignisse korreliert mit den Dehnungszuwächsen $\Delta\varepsilon = 0.08‰$ (hier bezeichnet als: globale diskrete Ereignisrate) der Prüfkörper I bis IV *a–d*; mitangegeben ist die globale kummulative SE Ereigniskurve und der globale Spannungs-Dehnungszusammenhang

of global AE events vs. strain or stress incorporate a high uncertainty for prediction of failure resp. for description of critical damage accumulation.

The mentioned non-linearity of the global stress-strain curve equally encountered for all four specimens, showing a very early deviation from linearity at roughly 0.20 F_u, is not correlated with the rate of acoustic emissions, at least above the encountered noise level. Further investigations not presented in this paper revealed that the non-linearity effect stems from very early creep, and hereby primarily from shear creep.

A considerable improvement in the detection of a significant change in the AE rate and thus of the evolution of progressive micro-damage, assumed to be associated with the bursts, is obtained by consideration of local AE event rates and respective local cumulative AE event functions. Figures 11a–d show, analogous to Figs. 10a–d, the local AE event rates and respective cumulative curves, now exclusively comprising the acoustic emissions generated resp. localised within a bandwidth of ±8 mm around the failure plane. It can be seen that a considerably better estimation of a change of the AE rate resp. of the cumulative event slope is obtained for all specimens, except for No I, which showed already at the global level an unambiguous rate change. Especially in case of specimen II, where the global rate history did not forward clear indications of a change of the AE activity, the cumulative curve now can be well approximated bilinear, delivering strain resp. stress threshold values of 80 resp. 90% for accelerated damage.

For prediction of failure planes resp. of failure onsets, an evaluation of the event density development of AE clusters, i.e. of finite areas with increased spatial AE density, identified at lower load regimes, is promising. This is shown exemplarily for the clusters of specimen II indicated in Fig. 9b. Figure 12 gives for the whole loading regime the local cumulative AE event curves of the four localised event clusters CL1 to CL4 normalised by the respective cluster area. The graph reveals that the rate resp. slope changes of the cumulative curves of the different clusters allow a proper tracing of the spatial and loading dependent damage evolution process. Whereas the curves of clusters CL1, CL3 and CL4 exhibit only minor changes above 80% of ultimate load, the normalised cumulative event rate of cluster CL2, being in the vicinity of the failure plane, shows a pronounced rather constant increase between 0.83 F_u and failure load.

So local(ised) AE rates as related to stress or strain enable deeper insight in the complex damage evolution process for the brittle failure of spruce in tension perpendicular to the grain.

10 Conclusions

The results of the described AE tests with spruce in tension perpendicular to the grain support the assumption that acoustic emission in case of the specific material load combination may be generated mainly by some kind of

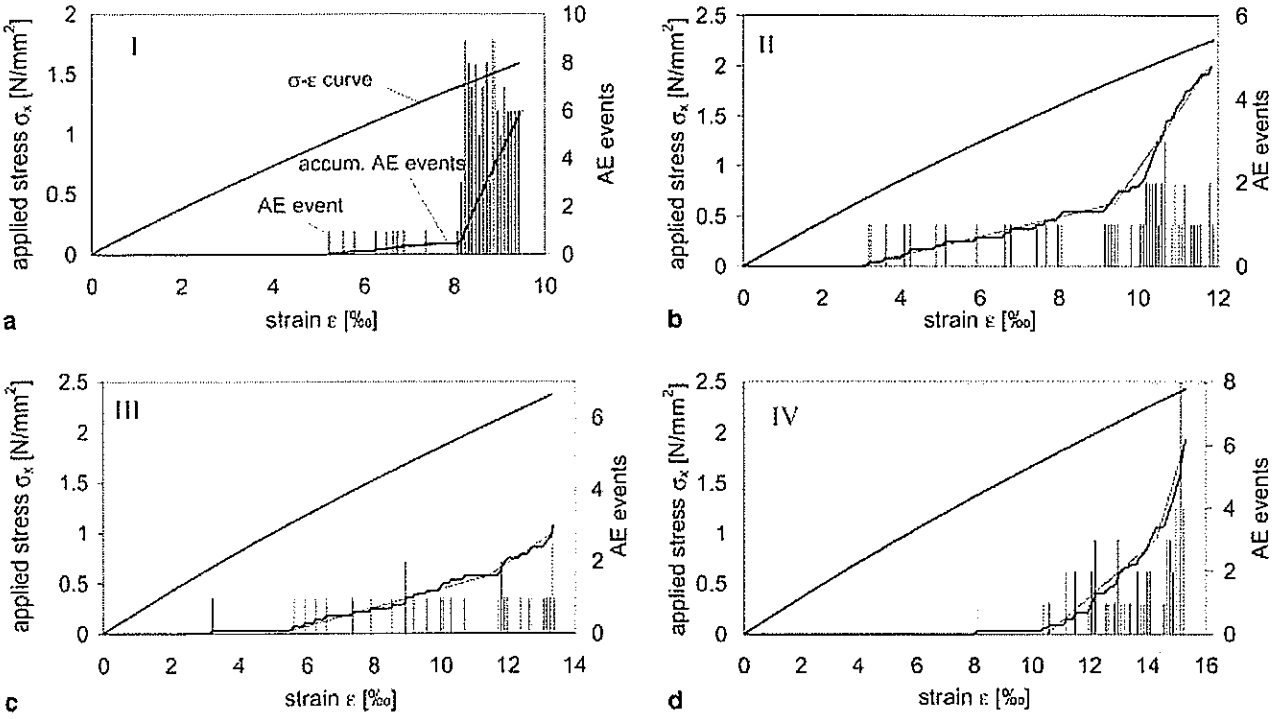

Fig. 11a–d. AE events located within a band of ±8 mm of the failure plane per strain increment $\Delta\varepsilon = 0.08‰$ (termed: local discrete AE event rate) of specimens I to IV *a–d*; also given are local cumulative AE event curve and global stress-strain curve

Bild 11a–d. SE Ereignisse lokalisiert innerhalb eines Bandes von ± 8 mm um die Bruchebene korreliert mit den Dehnungszuwächsen $\Delta\varepsilon = 0.08‰$ (hier bezeichnet als: lokale diskrete SE Ereignisrate) der Prüfkörper I bis IV *a–d*; mitangegeben ist die lokale kummulative SE Ereigniskurve und der globale Spannungs-Dehnungszusammenhang

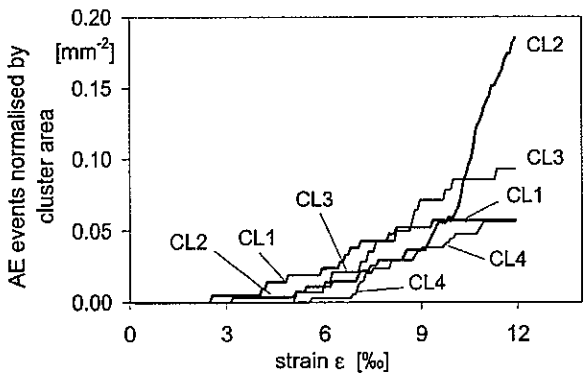

Fig. 12. Cumulative curves of local AE events normalised by cluster area of discrete event clusters of specimen II
Bild 12. Clusterflächen-normierte lokale kummulative SE Ereigniskurven von ausgezeichneten Ereignis-Clustern des Prüfkörpers II

micro-damage (micro-cracking). Obviously the damage processes indicated by the maximum of AE rates which occurred near the later failure plane did not change the global specimen stiffness.

The fact that the located burst emissions finally coincide for all specimens near the on-set of the respective failure plane can be taken as a prove that micro-damage, not detectable at the macro-scale through stiffness changes, causes acoustic emissions, i.e. AE signals can be taken as damage indicators of progressive damage.

References

Adams R D (1969) Fracture development in wood resulting from bending stresses and detected using the acoustic emission technique. Master thesis, University of British Columbia, Canada

Aicher S, Dill-Langer G (1996) Influence of cylindrical anisotropy of wood and loading conditions on off-axis stiffness and stresses of a board in tension perpendicular to the grain. Otto-Graf-J., 7:216–241, Otto-Graf-Institute, University of Stuttgart, Germany

Aicher S, Dill-Langer G (1999) Fracture location by NDT in glulam loaded in tension perpendicular to the grain. Proc. 11th Int. Symp. Nondestructive Testing of Wood:43–54, Forest Products Soc., Madison, USA

Aicher S, Dill-Langer G, Höfflin L (2001) Effect of polar anisotropy of wood loaded perpendicular to grain. J of Materials in Civil Eng, ASCE, 13: 2–9

Baron JA, Ying SP (1987) Acoustic emission source location. in: Acoustic Emission Testing, Nondestructive testing handbook (2nd ed.), vol. 5, Miller RK, McIntire P (ed) American Society for Non-destructive Testing

Becker HF (1982) Acoustic emissions during wood drying. Holz Roh-Werkstoff 40: 345–350

Booker JD (1994) Acoustic emission and surface checking in Eucalyptus regnans boards during drying. Holz Roh- Werkstoff 52: 383–388

Dill-Langer G, Aicher S (1997) Damage modelling of glulam in tension perpendicular to grain in variable climate. Int. Council Building Research Studies and Documentation, Working Commission W18, Proc. Meeting 30, paper CIB-W18/30–9–2, Vancouver, Canada

Dill-Langer G, Lütze S, Aicher S (in press) Microfracture in wood monitored by confocal laser scanning microscopy. Accepted for publication in Wood Sci Technol
Honeycutt RM, Shaar C, Simson WT (1985) Use of acoustic emissions to control drying rate of red oak. For Prod J 35: 48–50
Lee S-H (1994) Recognition of acoustic emission patterns from mixed mode wood fracture. Ph D. thesis, University of California, Berkeley, USA
Schniewind AP, Quarles SL, Lee S-H (1996) Wood fracture, acoustic emission and the drying process. Part. 1. Acoustic emission associated with fracture. Wood Sci Technol 30: 273–281
Sison M, Duke JC, Lozev MG, Clemena GG (1998) Analysis of acoustic emissions from a steel bridge hanger. Research in Nondestructive Evaluation 10: 123–145